Machine-learning-enabled geometric compliance improvement in two-photon lithography without hardware modifications

Yuhang Yang [a], Varun A. Kelkar [b], Hemangg S. Rajput [a], Adriana C. Salazar Coariti [c], Kimani C. Toussaint Jr [c], Chenhui Shao [a,*]

[a] *Department of Mechanical Science and Engineering, University of Illinois at Urbana-Champaign, Urbana, IL 61801, United States*
[b] *Department of Electrical and Computer Engineering, University of Illinois at Urbana-Champaign, Urbana, IL 61801, United States*
[c] *School of Engineering, Brown University, Providence, RI 02912, United States*

ARTICLE INFO

ABSTRACT

In recent years, two-photon lithography (TPL) has emerged as a practical and promising micro- and nano-fabrication technique for a wide range of applications. Numerous studies have reported improving the process control and printed feature size of TPL, including by incorporating some degree of hardware improvements, which may be prohibitive for commercial systems. However, the geometric accuracy of TPL-fabricated 3D structures has not been well understood. In this study, a general machine-learning-based framework is presented to quantitatively model and improve the geometric compliance in TPL. The framework quantifies the spatial variation in geometric compliance of fabricated 3D structures, and then designs compensation strategies to improve the geometric compliance. Two experimental case studies, one at the microscale and the other at the nanoscale, are presented to demonstrate the effectiveness of the framework. It is revealed for the first time that systematic geometric errors exist in TPL-fabricated structures and such errors exhibit a strong spatial correlation. The produced compensation strategies reduce the average errors in key geometric features at the microscale and nanoscale by up to 79.7% and 47.4%, respectively. The case studies demonstrate that the proposed framework can effectively improve the geometric compliance without introducing any modifications to the hardware or process parameters, thereby facilitating more widespread adoption.

1. Introduction

Two-photon lithography (TPL) is an additive manufacturing (AM) technique based on laser scanning that is well-suited for rapidly prototyping 3D micro and nano structures, the demand for which has sky-rocketed over the years due to application in many disparate and broad fields such as electronics, medicine, communications, and optics [1–3]. In TPL, a high intensity ultrafast laser beam is tightly focused inside a photo-reactive polymer, which leads to polymerization or scission due to two-photon absorption occurring in the high-intensity region of the focal volume [4]. 3D fabrication using TPL was first demonstrated in 1997, and has been shown to routinely produce structures on the order of a few hundred nanometers [5]. Improvements in the resolution have been achieved by various methods including controlling the process parameters such as laser power, exposure time, and the numerical aperture of

the objective [6–8].

Although TPL has an impressive capability to create complex microscale and nanoscale 3D structures, the produced structures show a large variability in the geometric compliance due to the intricate physical and optical phenomena involved, including shrinkage [9], deformation [10], shape distortion [11], and step effect [12–15]. The geometric compliance is an important quality attribute. It is directly related to the mechanical and optical properties of TPL-produced structures, and these properties govern the performances and functionalities of produced structures, such as micro-lenses [13,16], micro-needles [17], and microfluidic devices [18]. Hence, it is crucial to quantitatively investigate the geometric variability and improve the geometric compliance of structures produced by TPL.

Significant research gaps still exist in the characterization, modeling, and control of the geometric compliance of TPL-fabricated structures.

First, there is a lack of research on quantitative, fine-scale assessment of the geometric compliance of TPL-produced 3D structures. A few recent studies have focused on the process control and geometric compliance of TPL. Zhou et al. reviewed several factors influencing the processing accuracy in TPL, such as the step effect caused by 3D motion of the laser beam, the inherent errors between the stereolithography file and the designed model, and shrinkage/deformation due to low mechanical strength during the developing process [19]. They also discussed approaches to potentially improve the process accuracy, including increasing the overlap of the illumination voxel, controlling the scanning direction, and changing the layer thickness. LaFratta and Baldacchini reviewed methods for analyzing and characterizing the mechanical and chemical properties of fabricated microstructures [20]. However, none of the existing studies precisely measured or analyzed the 3D geometric accuracy. Some works acquired dimensional information from scanning electron microscope (SEM) images, but such information did not adequately capture the 3D geometric accuracy [17,21]. Since TPL is essentially an AM technique for producing 3D structures with nearly arbitrary geometries, quantitative evaluation and analysis of dimensional accuracy are crucial for moving TPL from laboratory to industrial scale.

Second, the potential of leveraging the recent advancement in data science to enable the modeling and control of geometric compliance in micro- and nano-scale AM processes is largely untapped. There have been rich studies on macro-scale AM using data science techniques. Some research focuses on in-situ sensing technologies and data-driven process monitoring methods. For example, different data-driven models have been developed to monitor and control the layer width or roughness for wire arc AM [22–24] and fused filament fabrication [25,26]. Some studies used thermal imaging to detect process abnormalities in direct laser deposition [27–30]. Meltpool emission monitoring was used to monitor the quality of porous structures produced by laser powder bed fusion [31]. Machine learning has been used to establish the process–structure–property relationships in design for AM [32,33]. A few publications have focused on the prediction and control of geometric variability in printed parts by analyzing the CAD models and comparing with models of machine capabilities. Data-driven models such as statistical models [34,35], cookie-cutter model [36], Gaussian process [37], and Bayesian neural network [38] have been used to characterize and compensate geometric deviations. Additionally, systems-level investigation of variability in geometric features of lattice parts made on multiple machines demonstrated the existence of machine-to-machine variability [39]. Despite that a rich body of literature on macro-scale AM exists, there is a lack of studies on using data science to improve geometric compliance in micro- and nano-scale TPL.

To date, the TPL process variability has been neither systematically investigated nor quantitatively modeled, not to mention controlling the variability. To fill the research gaps, in this study, a machine-learning-based framework is developed to both quantitatively characterize and improve the geometric compliance of micro- and nano-scale TPL processes. Specifically, Gaussian process (GP) regression is utilized to model the spatially varying trends of the geometric deviations between structures. A data-driven compensation approach to reduce the geometric deviations is presented. The remainder of this paper is organized as follows. The proposed modeling and decision-making framework are first introduced. The experimental setup and 3D characterization techniques are then presented for two different designs including a microscale hemisphere and a nanoline. The patterns of geometric deviations in TPL processes are discussed and the effectiveness of the proposed framework is showcased, followed by a discussion on the limitations of the proposed framework and potential future research directions. An open-source software tool developed based on the proposed framework can be accessed online [40].

2. Modeling and decision-making framework

A schematic of the proposed framework is shown by Fig. 1. Existing practice often uses a one-way approach and does not quantitatively assess the geometric quality of fabricated structures. In a typical workflow, a user designs a 3D structure using CAD software. The CAD model is then transferred to a TPL machine, and a 3D structure is fabricated. Though qualitative quality check, e.g., using SEM [17,21], is sometimes used, quantitative assessment of the geometric quality is often lacking. Here, the proposed framework closes the loop by using 3D metrology and developing learning and decision-making capabilities. The geometric measurements are first obtained using 3D metrology. The dimensional quantities of the geometric elements are referred to as geometric features, and the controllable features are the dimensions that can be set up directly in the CAD design. In the learning stage, the geometric features in individual structures as well as their spatial distributions are quantified using GP regression [41]. Lastly, the machine-learning-enabled decision-making algorithm prescribes an optimal CAD design that can achieve the best geometric compliance by compensating the systematic errors. The structures reproduced with the compensated design under the same manufacturing settings would have a minimal deviation from the desired feature value. In the remainder of this section, the proposed modeling and decision-making methods are elaborated.

2.1. Learning and modeling geometric variability

GP regression is selected to model the geometric variability of TPL-fabricated structures because it has demonstrated excellent capability for spatial analysis in various manufacturing applications [42–49]. GP regression is able to adequately capture the spatial variability exhibited in the TPL problem. It should be noted that other regression methods may be preferred for the modeling task if the variability pattern is different.

In a GP regression model, let $\mathbf{s}_i$ be a coordinate vector representing the spatial location of the i-th structure on one sample and $D_\mathbf{s} = \{\mathbf{s}_1, \ldots, \mathbf{s}_n\}$ denote the set of spatial locations for all n structures on the sample. The following assumptions are made regarding the proposed modeling approach.

1. Each geometric feature in the model is independent. The controllable features studied in this paper do not exhibit strong correlations with each other. When a strong correlation exists between the geometric features, multivariate regression can be used to account for the correlations.

2. The measurements of the actual fabricated structures can be linearly approximated by a function of the spatial location. In other words, at location $\mathbf{s}$, the measurement of a geometric feature, $Z(\mathbf{s})$, is proportional to the value in the design, $Y(\mathbf{s})$, by a scale factor, $f(\mathbf{s})$. Such a linear relationship is expected because the geometric errors are accumulated during the point-by-point, line-by-line, and layer-by-layer fabrication in AM processes [50,51].

Based on these assumptions, the proposed spatial model can be expressed by the following equation:

$$Z(\mathbf{s}) = Y(\mathbf{s})f(\mathbf{s}) + \varepsilon, \tag{1}$$

where $Y(\mathbf{s})$ is the value of the feature at location $\mathbf{s}$ in the design, $f(\mathbf{s})$ is the spatial function that maps the value in the design to the measurement of the actual fabricated structures, and ε is a zero-mean error with variance σ. f reflects the systematic error, representing the consistent and repeating spatial trends. ε characterizes the random error, which is caused by the inherent process variability.

Measurement data are used to learn the function f. The link function $f(\mathbf{s})$ can also be formularized in other forms, depending on what variability patterns exist in the targeted problem. In this study, the function f is modeled as a GP and is specified by a constant mean m and the
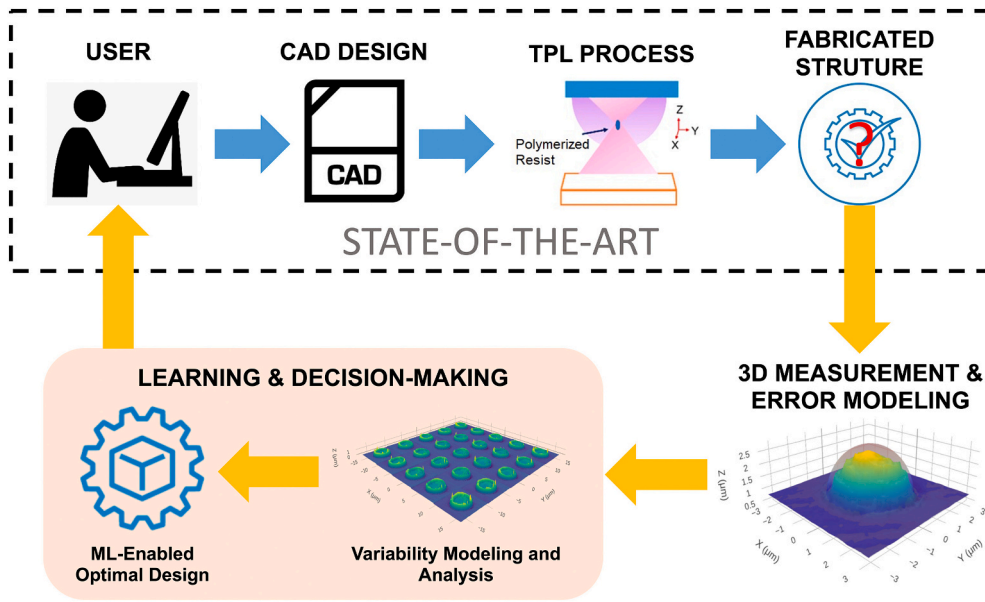
Fig. 1. The proposed framework for characterizing geometric variability and improving geometric compliance in TPL.

covariance function $\kappa(\mathbf{s}, \mathbf{s}')$:

$$f(\mathbf{s}) \sim \mathcal{N}(m, \kappa(\mathbf{s}, \mathbf{s}')),$$
$$\kappa(\mathbf{s}, \mathbf{s}') = \mathbb{E}[(f(\mathbf{s}) - m)(f(\mathbf{s}') - m)]. \tag{2}$$

Here, the implementation of GP regression is briefly summarized in the context of geometric feature modeling in TPL. More details on the theory and other applications of GP can be found in [41,52]. The prior on the noisy observations is

$$cov(\mathbf{Z}) = Y(\mathbf{S})^{\mathsf{T}} K(\mathbf{S}, \mathbf{S}) Y(\mathbf{S}) + \sigma_\varepsilon^2 \mathbf{I}, \tag{3}$$

where $\mathbf{S}$ is a matrix representing a set of all relative spatial locations in $D_{\mathbf{s}}$ and $K(\mathbf{S}, \mathbf{S})$ is the covariance matrix with elements corresponding to the covariance function $\kappa(\mathbf{s}, \mathbf{s}')$. The squared exponential kernel, one of the most commonly used kernels, is used in this study [41,52], and the Broyden-Fletcher-Goldfarb-Shanno (BFGS) method is used to estimate the kernel parameters [53].

The measurement of the actual fabricated structures $\mathbf{Z}$ at spatial locations $\mathbf{S}$ and the estimated values $\mathbf{Z}_*$ at a given set of unmeasured locations $\mathbf{S}_*$ follow the following joint distribution

$$\begin{bmatrix} \mathbf{Z} \\ \mathbf{Z}_* \end{bmatrix} \sim \mathcal{N} \left(m\mathbf{I}, \begin{bmatrix} \mathbf{Y}^{\mathsf{T}} K(\mathbf{S}, \mathbf{S}) \mathbf{Y} + \sigma_\varepsilon^2 \mathbf{I} & \mathbf{Y}^{\mathsf{T}} K(\mathbf{S}, \mathbf{S}_*) \mathbf{Y}_* \\ \mathbf{Y}_*^{\mathsf{T}} K(\mathbf{S}_*, \mathbf{S}) \mathbf{Y} & \mathbf{Y}_*^{\mathsf{T}} K(\mathbf{S}_*, \mathbf{S}_*) \mathbf{Y}_* \end{bmatrix} \right), \tag{4}$$

where $\mathbf{Z}_* = \mathbf{Y}_* \mathbf{f}_*$, $\mathbf{Y} = Y(\mathbf{S})$, $\mathbf{Y}_* = Y(\mathbf{S}_*)$, $\mathbf{f} = f(\mathbf{S})$, and $\mathbf{f}_* = f(\mathbf{S}_*)$. The derived predictor at a single spatial location $\mathbf{s}_*$ can be expressed as

$$\widehat{f}(\mathbf{s}_*) = m + \sum_{i=1}^{n} \kappa(\mathbf{s}_i, \mathbf{s}_*) \left[\mathbf{Y}^{\mathsf{T}} K(\mathbf{S}, \mathbf{S}) \mathbf{Y} + \sigma_\varepsilon^2 \mathbf{I} \right]^{-1} Z(\mathbf{s}_i). \tag{5}$$

It should be noted that the value of function at a single location $\mathbf{s}$, such as $f(\mathbf{s})$, $Z(\mathbf{s})$, and $Y(\mathbf{s})$, is a scalar, while $\mathbf{f}/f(\mathbf{S})$, $\mathbf{Z}/Z(\mathbf{S})$, and $\mathbf{Y}/Y(\mathbf{S})$ are vectors representing the values at a set of locations $\mathbf{S}$.

2.2. Generating compensation designs

With a geometric variability model, the feature value of a fabricated structure at location $\mathbf{s}$, $Z(\mathbf{s})$, can be predicted given the designed feature value, $Y(\mathbf{s})$. The controllable geometric features, such as length, height, and radius, can be changed to optimize the geometric compliance. The feature value in the compensated design, $Y_c(\mathbf{s})$, should make the resulting fabricated structure, $Z_c(\mathbf{s})$, closer to the desired feature value,

$Y_d(\mathbf{s})$. In the proposed compensation approach, $Y_c(\mathbf{s})$ is a discrete variable determined by the TPL machine precision, p. The machine precision is the minimal step of z-axis movement and it is determined by the capability of the fabricating system. For Nanoscribe GT used in this study, the machine precision is 100 nm, which is the minimal motion unit that can be handled by numerical control programming. In other words, the features in design must be a multiple of 100 nm or the residual does not affect the fabrication process. For example, 500 nm and 530 nm in design will be processed as 500 nm. Hence, $Y_c(\mathbf{s})$ should be a multiple of the machine precision.

The feature value in the compensated design $Y_c(\mathbf{s})$ can be obtained by reversely calculating the desirable feature value and be expressed as:

$$Y_c(\mathbf{s}) = r\left(\frac{Y_d(\mathbf{s})}{f(\mathbf{s})}, p \right), \tag{6}$$

where $r(x, p) = \lfloor \frac{x}{p} \rceil \times p$ is a function that rounds x to a multiple of p, and $\lfloor \bullet \rceil$ denotes an integer rounding function such that $\lfloor x \rceil$ is the nearest integer that x is rounded to. Function r ensures that $Y_c(\mathbf{s})$ is a multiple of the machine precision that would lead to a measurement of compensated structure $Z_c(\mathbf{s})$ with a minimal deviation from the desired feature value $Y_d(\mathbf{s})$. In other words, the feature value in the compensated design, $Y_c(\mathbf{s})$, is determined by $f(\mathbf{s})$ and p. This compensation approach provides us with the ability to control the TPL process at multiple scales.

3. Experiments

In this section, we first present the experimental settings and then the designs of structures at micro and nano scales. The details of the 3D measurements systems and structure characterization approach are also discussed.

All experimental structures are manufactured with a commercial TPL system (Photonic Professional GT, Nanoscribe GmbH). A femtosecond fiber-laser of center wavelength 780-nm and repetition rate 80-MHz is focused using a 1.4 numerical aperture (NA) 63× Oil DIC objective (Zeiss, Plan Apochromat) onto a drop of 0.05-ml photosensitive polymer (IP-Dip, Nanoscrib GmbH) placed on a 1-in. × 1-in. fused silica substrate. The laser power is set as 50 mW and scanning frequency is set as 30 kHz. The entire 3D structure is built by scanning the voxel in the x-, y-, and z-directions. The focus is initially located at the interface between the substrate and the photoresist, and it is scanned with the help of galvo

mirrors in the *x-y* plane. At each focus, the photoresist is polymerized due to two-photon polymerization induced by the high intensity of the laser. A piezoelectrically activated stage holding the sample achieves the relative motion of the focus spot with respect to the sample in the *z*-direction.

We carry out our study using two designs—hemispheres at the microscale and nanolines at the nanoscale. These two geometric designs are selected for the case studies because they have been widely used, either directly or as building blocks for complex structures, in a wide range of applications, including micro-optics [13,16,54], microfluidic devices [18,55], and micro electromechanical systems [21,56]. Investigating the geometric variability in the chosen structures will allow us to better evaluate the properties of the produced structures and improve their performances and functionalities in these manufacturing applications. The schematic representations of the geometric designs are displayed in Fig. 2. Forty samples of the microscale hemisphere structures are fabricated, measured, and characterized in the learning stage, where the sample measurements are used as the training dataset to fit the model parameters. The designed radius of each hemisphere is 2 μm. In each sample, 25 such structures are evenly spaced on a 5 × 5 grid on the base box of dimensions 40 μm × 40 μm × 3 μm. For the nanoscale line structures, eight samples are fabricated, measured, and characterized in the learning stage. The dimensions of the nanolines are selected as 20-μm length, 500-nm thickness, and 500-nm height. Each sample consists of 13 lines on a 40-μm × 40-μm × 3-μm base box.

A 3D laser scanning confocal microscope (VK-X1000, Keyence), equipped with a 150× objective lens, is used to measure the microscale hemisphere structures. It can acquire both an optical image and a high-resolution surface profile over an area of 123 μm × 92 μm with 1-nm vertical resolution and 100-nm lateral resolution. Atomic force microscopy (AFM) (Tosca 400, Anton Paar) is employed to measure the geometry of the nanolines. It can achieve one angstrom vertical resolution and the lateral resolution is set as 20 nm.

4. Results

In this section, we analyze the patterns of geometric deviations in TPL processes and demonstrate the effectiveness of the proposed data-driven compensation method. The case study with microscale hemispherical structures is discussed first, followed by the case study with nanoscale line structures.

Fig. 3 shows the SEM images of fabricated structures. It is impossible to get accurate geometric information from the SEM image to reveal and quantify the differences between the fabricated structures with the same design. Hence, high-resolution 3D metrology is necessary for quantitative characterization of the geometric compliance in TPL.

4.1. Microscale hemispherical structure

The goal of the quantitative analysis is to characterize the geometric features of the structures and use GP regression to model the spatially varying trends of the geometric deviations between structures. The first step toward this goal is identifying the region of interest on the surface

profile and extracting the geometric information from each structure. For the hemisphere structures, height, equivalent radius, and volume are identified as the three key geometric features. The 3D visualization of geometric measurement for one single hemisphere and the spatial trend of geometric features in forty samples are shown in Fig. 4. Compared with the structures on the edges, the structures near the center have equivalent radius and volume 2.8% and 6.5% larger on average, respectively. The patterns of geometric deviations between structures are spatially correlated. In addition, it can be noticed that three geometric features, height, radius, and volume, are 16.9%, 3.4%, and 37.2%, smaller than the desired values in design, respectively.

Height and radius are two controllable geometric features for the hemisphere structures, while volume, as a 3D feature, cannot be set up directly in CAD designs. It should be noted that height is not strongly correlated with radius ($r^2 = 0.11$) or volume ($r^2 = 0.33$) and only radius and volume are strongly correlated ($r^2 = 0.91$). Hence, height and radius are modeled independently. For each feature, a GP model is built with data of 1000 structures from 40 samples. A compensated CAD design is generated with the built GP model using the proposed approach, where the feature values varies at different locations in the compensated design. Ten samples are produced with the compensated design under the same manufacturing settings. The statistics of the geometric features in the original design and in the compensated design are listed in Table 1. The spatial trends of the errors in geometric features are displayed in Fig. 5. With the proposed compensation approach, the average errors in height, equivalent radius, and volume are reduced by 73.0%, 79.7%, and 29.4%, respectively. It is noticed that not only the average values of the geometric features are closer to the desired values, but also the relative standard deviation (RSD) is smaller. RSD, also known as the coefficient of variation, is calculated as [57].

$$\text{RSD} = \frac{\sigma}{|\mu|} \times 100\%, \tag{7}$$

where σ is the standard deviation and μ is the mean. It reflects the variability relative to the mean. In this study, a smaller RSD indicates a reduced intra-sample variability and an improved process repeatability. Although the standard deviation of height in compensated design is slightly higher than in the original design, the average height increases more, leading to a smaller RSD.

4.2. Nanoline structure

An array of nanolines are fabricated and used to demonstrate the effectiveness of the proposed framework at the nanoscale. Fig. 6a presents an AFM image for one sample with nanolines. A line profile of the 13-line structures is provided in Fig. 6b. It is observed that the nanoline structures near the center are higher than those on the edges and the base box surface is curved. In the geometric measurements, the nanoline structures are extracted from the curved surface and the line height is identified as the key geometric feature. It should be noted that the precision of the instrument, which is the minimal distance between two adjacent layers, is 100 nm, and the feature size-to-precision ratio would be only 5 for the structure with feature size of 500 nm. Such a small
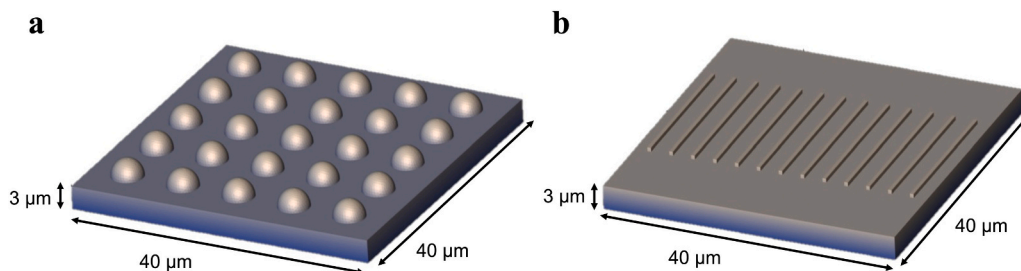

Fig. 2. Schematic representations of the geometric design. (a) hemispheres. (b) nanolines.
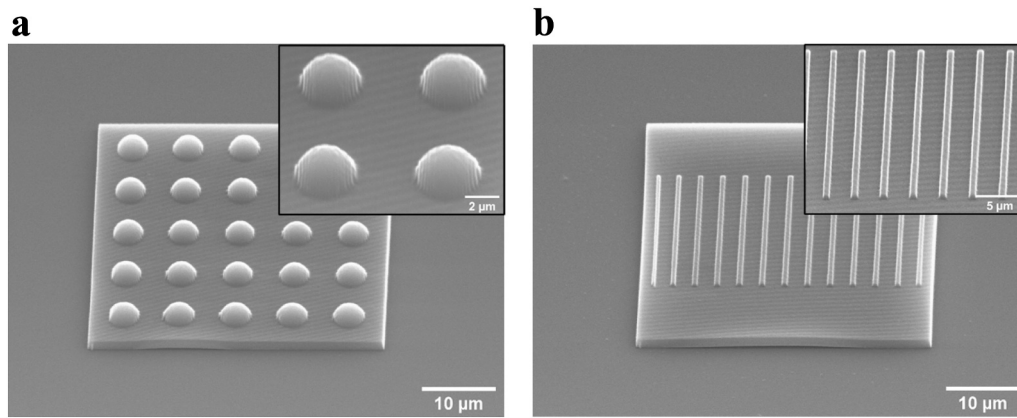
Fig. 3. SEM images of fabricated structures. (a) hemispheres. (b) nanolines. The fabricated structures with the same design looks almost identical in the SEM image.
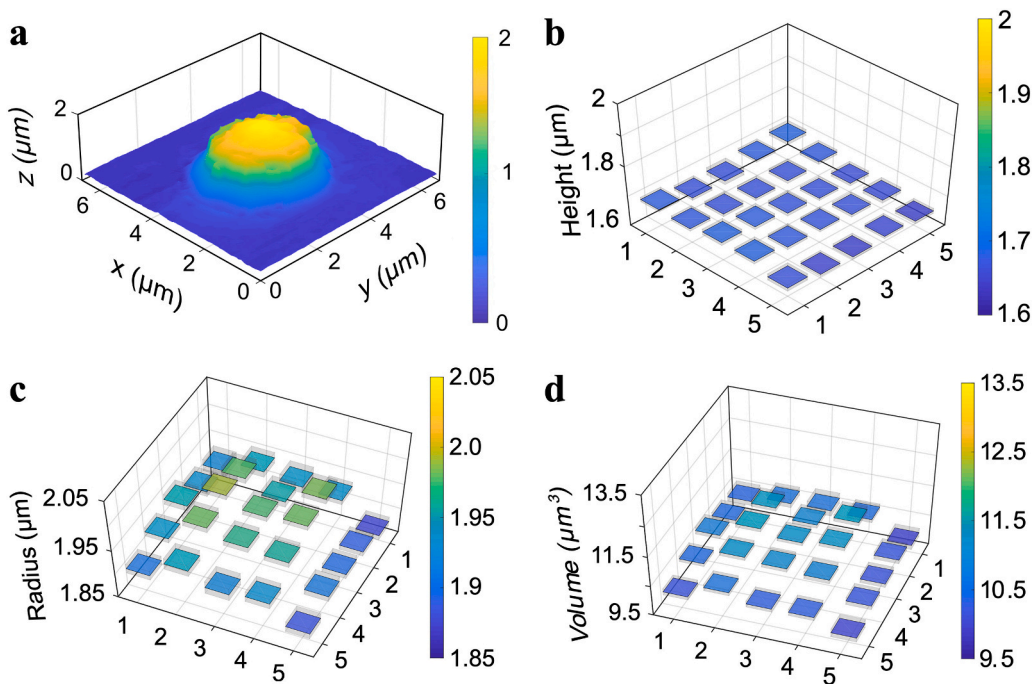

Fig. 4. Quantitative characterization of the hemisphere structures fabricated with the original design. (a) 3D visualization of geometric measurement for an individual hemisphere. Spatial trends of geometric features (b) height (c) equivalent radius (d) volume. The *x*-axis and *y*-axis in (b) (c) (d) are relative locations of the structures.

Table 1
The average values ± standard deviations, average errors, and RSD of the geometric features of the hemisphere structures produced with the original design and with the compensated design.

		Desired	Original	Compensated
Height	Avg. ± Std. (μm)	2.000	1.671 ± 0.020	1.912 ± 0.022
	Avg. error (μm)	NA	0.329	0.088
	RSD	NA	1.20%	1.17%
Radius	Avg. ± Std. (μm)	2.000	1.933 ± 0.036	1.987 ± 0.023
	Avg. error (μm)	NA	0.067	0.013
	RSD	NA	1.88%	1.16%
Volume	Avg. ± Std. (μm³)	16.755	10.520 ± 0.438	12.355 ± 0.331
	Avg. error (μm³)	NA	6.235	4.400
	RSD	NA	4.17%	2.68%

feature size-to-precision ratio poses a fundamental limit to geometric accuracy, and the data-driven compensation approach can lead to a minimal deviation from the desired feature in the compensated

structures even under such a limitation.

A GP model is built using the measured heights of 104 structures from eight samples. Four samples are produced with the compensated height under the same manufacturing settings. The statistics of the measured heights of structures produced using the original design and compensated design are listed in Table 2. The spatial trends of the average heights of the line structures in the original design and the compensated design are displayed in Fig. 6c. The average line height is 488.41 nm in the original design and 506.10 nm in the compensated design. With the compensation approach, the average height is closer to the desired value and the average error in height is reduced by 47.4%.

It should be noted that the base box surfaces are curved as shown in Fig. 6b, which might be caused by the surface tension and internal stress in the liquid solidifying processes. In order to characterize the geometric features of the structures of interest, it is important to first extract the region of each structure in the surface profile. A robust approach to extracting the regions of structures from the surface profile is developed. The contours of the structures are identified using Canny edge detector
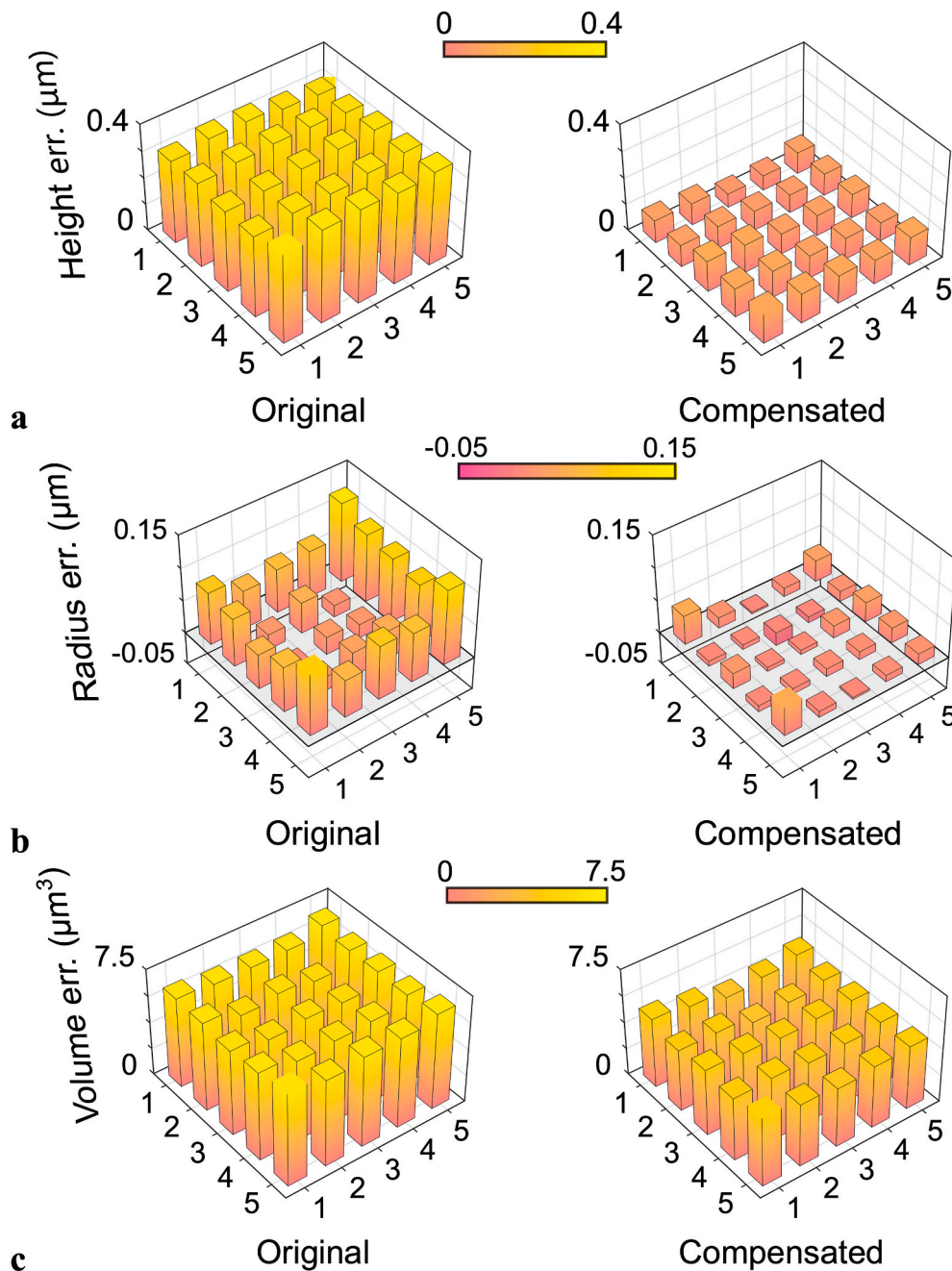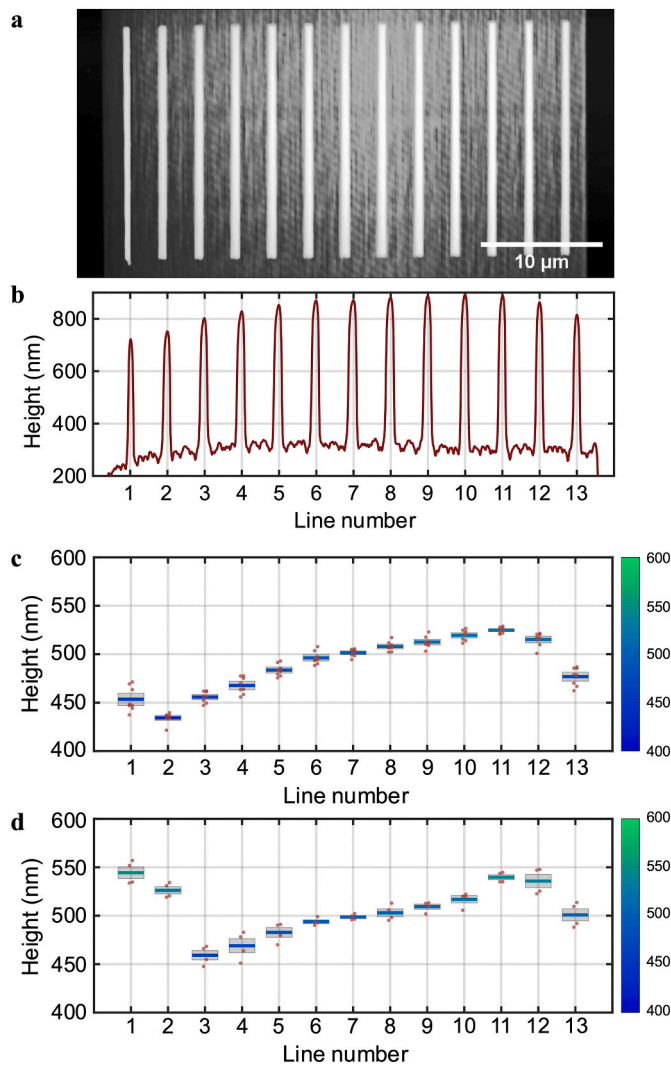
Fig. 5. The spatial trends of the errors in geometric features before and after compensation. (a) height (b) equivalent radius (c) volume. The errors in all three features are significantly reduced with the compensation approach. The *x*-axis and *y*-axis are relative locations of the structures.

[58]. Sobel operator is utilized to estimate the intensity of the gradients in the surface profile [59]. Since closed contours are required for the structure extraction, morphological filters and binary image operations are adopted to close the open borders. Compared with simple region extracting approaches, the edge-detection-based method can robustly extract the region of each structure well even when the base box surfaces are curved. For example, using a single height threshold to "cut off" the structures from the base box is also a region extracting method. However, with such a method, we either miss lower portions of the structures near the base box surface or include redundant parts from the base when the base box surfaces are curved.

5. Discussion

Our proposed framework consists of three important components—(1) high-resolution quantitative image characterization, (2) machine-learning-based modeling that captures the geometric variability, and (3) a data-driven compensation algorithm. The effectiveness of the framework has been proven by experimental case studies with micro-scale hemispherical structures and nanoscale line structures. Without introducing any hardware improvements or changing the process parameters, the compliance of geometric features with their designed values is significantly improved across the board under the precision limit from the hardware.

The goal of the geometric variability modeling is to predict the values of actual geometric features using the spatial locations of given

Fig. 6. Nanoline structures. (a) AFM image. (b) A profile across the midpoints of the 13 nanoline structures. (c, d) The spatial trends of the average heights of the line structures before and after compensation, respectively. The error bars represent the standard deviations.

Table 2
The average values ± standard deviations, average errors, and RSD of the heights of the line structures produced with the original design and with the compensated design.

	Desired	Original	Compensated
Avg. ± Std. (nm)	500.00	488.41 ± 28.50	506.10 ± 26.63
Avg. error (nm)	NA	11.59	6.10
RSD	NA	5.84%	5.26%

structures. Due to the complex nature of the polymerization process, it is challenging to predict the complex patterns of shrinkage, deformation, and other internal/interfacial defects developed during the TPL process with a descriptive physical model. Different from other machine-learning-based regression techniques, GP regression is based on statistical models capturing both autocorrelation and the statistical relationships among the spatial locations, which are usually described by kernels or covariance functions. Taking advantage of the spatial correlation, GP regression can achieve a better predictive performance for the complex nonlinear relationships between spatial locations and geometric features. In addition, GP is much more data efficient than some other machine learning methods such as deep neural networks, making

it particularly suitable for TPL applications, where data scarcity is identified as a key challenge.

Our observations suggest that the geometric variability in TPL manifests in the forms of both systematic and random errors. We anticipate that such errors are determined by some other factors, but to focus on a tractable problem, we only investigate the effect of the spatial locations in this study. Here, we suggest a few future research directions. First, the influence of process parameters such as the average power of the femtosecond laser, exposure time, and photo-initiator materials on the geometric compliance is worth investigating. Existing theoretical and experimental studies have shown that these process parameters can affect the dimensions of voxels, the fundamental unit of TPL, and influence the process accuracy [19]. In addition, it has been reported that the optical, environmental, and material parameters also affect the geometric deviations [19,20]. Investigating the influence of process parameters may also advance the physical understanding on the sources of TPL process variability and the fundamental limit of TPL process capability.

Hybrid modeling with GP, also known as additive GP or integrated GP, can be potentially used to model the spatial variability with a trend dominated by these process parameters [45,46,60–63]. The predicted geometric feature at location **s** with a set of process parameters **β** can be expressed as:

$$Z(\boldsymbol{\beta}, \mathbf{s}) = \mu(\boldsymbol{\beta}; Y(\mathbf{s})) + Y(\mathbf{s})f(\mathbf{s}), \qquad (8)$$

where $\mu(\boldsymbol{\beta}; Y(\mathbf{s}))$ is the expected feature value with process parameters **β** and designed feature value $Y(\mathbf{s})$. Instead of assuming a constant mean function, we model the mean as a function of both process parameters and desired design. This type of modeling scheme has proven effective in simultaneously characterizing a large-scale global trend dominated by physics and a small-scale residual reflecting natural variability in applications of additive manufacturing [63], high-precision machining [45,46], and ultrasonic metal welding [62].

Second, the effect of the laser scanning direction, which determines the order of the fabrication process, has not been investigated in the existing literature. In our study, we also fabricated the nanoline structures with a scanning direction rotated from the default value by 180°. Interestingly, the resulting spatial variability pattern is perfectly mirror symmetric to the trend resulting from the default scanning direction. This implies that the scanning direction is one of the factors that cause spatial variability. This asymmetric spatial variability and the underlying physical mechanism have not been reported in the literature. The proposed framework can be extended to help explain this phenomenon and further devise a compensation strategy.

Third, more efforts are needed to demonstrate the scalability and generalizability of the proposed framework. In this research, all structures in one sample have identical, and relatively simple designs and are uniformly allocated on the substrate. However, in practice, the geometric designs can be much more complicated. It is also worth investigating how varying the spatial distributions of the structures, e.g., with different spacing, will influence the variability patterns.

6. Conclusion

This paper presents a general machine-learning-based framework to quantitatively model and improve the geometric compliance in TPL. The existence of systematic and random geometric errors in TPL-fabricated structures is revealed for the first time. Without introducing any hardware improvements or changing the process parameters, the compliance of geometric features with their designed values is significantly improved across the board under the precision limit from the hardware. The average errors of the geometric features in the microscale and nanoscale structures are reduced by up to 79.7% and 47.4%, respectively, demonstrating a significant improvement in geometric accuracy. The independence of our approach to hardware improvements

facilitates widespread adoption as it is readily compatible for use with commercial systems. Drawing on this work, more sophisticated modeling and compensation methods may be developed for more complicated 3D designs by leveraging the advances in data science.

CRediT authorship contribution statement

Yuhang Yang: Conceptualization, Data curation, Formal analysis, Investigation, Methodology, Software, Validation, Visualization, Writing – original draft, Writing – review & editing. **Varun A. Kelkar:** Conceptualization, Data curation, Formal analysis, Investigation, Validation, Visualization, Writing – original draft, Writing – review & editing. **Hemangg S. Rajput:** Conceptualization, Data curation, Investigation, Validation, Writing – original draft, Writing – review & editing. **Adriana C. Salazar Coariti:** Conceptualization, Data curation, Investigation, Validation, Writing – original draft, Writing – review & editing. **Kimani C. Toussaint:** Conceptualization, Funding acquisition, Methodology, Supervision, Project administration, Writing – original draft, Writing – review & editing. **Chenhui Shao:** Conceptualization, Funding acquisition, Methodology, Supervision, Project administration, Writing – original draft, Writing – review & editing.

Declaration of competing interest

The authors declare that they have no known competing financial interests or personal relationships that could have appeared to influence the work reported in this paper.

Acknowledgment

References

[1] Geng Q, Wang D, Chen P, Chen S-C. Ultrafast multi-focus 3-D nano-fabrication based on two-photon polymerization. Nat Commun 2019;10(1):1–7.

[2] Vyatskikh A, Delalande S, Kudo A, Zhang X, Portela CM, Greer JR. Additive manufacturing of 3D nano-architected metals. Nat Commun 2018;9(1):1–8.

[3] Maddox S, Afshar-Mohajer M, Zou M. Digitization, replication, and modification of physical surfaces using two-photon lithography. J Manuf Process 2020;54:180–9.

[4] Boyd RW. Nonlinear optics. Academic press; 2019.

[5] Maruo S, Nakamura O, Kawata S. Three-dimensional microfabrication with two-photon-absorbed photopolymerization. Opt Lett 1997;22(2):132–4.

[6] Kawata S, Sun H-B, Tanaka T, Takada K. Finer features for functional microdevices. Nature 2001;412(6848):697–8.

[7] Tan D, Li Y, Qi F, Yang H, Gong Q, Dong X, Duan X. Reduction in feature size of two-photon polymerization using scr500. Appl Phys Lett 2007;90(7):071106.

[8] Dong X-Z, Zhao Z-S, Duan X-M. Improving spatial resolution and reducing aspect ratio in multiphoton polymerization nanofabrication. Appl Phys Lett 2008;92(9):091113.

[9] Sun H-B, Suwa T, Takada K, Zaccaria RP, Kim M-S, Lee K-S, Kawata S. Shape precompensation in two-photon laser nanowriting of photonic lattices. Appl Phys Lett 2004;85(17):3708–10.

[10] Yang D-Y, Park SH, Lim TW, Kong H-J, Yi SW, Yang HK, Lee K-S. Corrected article: "ultraprecise microreproduction of a three-dimensional artistic sculpture by multipath scanning method in two-photon photopolymerization"[appl. phys. lett 90, 013113 (2007)]. Appl Phys Lett 2007;90(7):079903.

[11] Liao C-Y, Bouriauand M, Baldeck PL, Léon J-C, Masclet C, Chung T-T. Two-dimensional slicing method to speed up the fabrication of micro-objects based on two-photon polymerization. Appl Phys Lett 2007;91(3):033108.

[12] Park SH, Lee SH, Yang D-Y, Kong HJ, Lee K-S. Subregional slicing method to increase three-dimensional nanofabrication efficiency in two-photon polymerization. Appl Phys Lett 2005;87(15):154108.

[13] Guo R, Xiao S, Zhai X, Li J, Xia A, Huang W. Micro lens fabrication by means of femtosecond two photon photopolymerization. Opt Express 2006;14(2):810–6.

[14] Wu D, Wu S-Z, Niu L-G, Chen Q-D, Wang R, Song J-F, Fang H-H, Sun H-B. High numerical aperture microlens arrays of close packing. Appl Phys Lett 2010;97(3):031109.

[15] Takada K, Sun H-B, Kawata S. Improved spatial resolution and surface roughness in photopolymerization-based laser nanowriting. Appl Phys Lett 2005;86(7):071122.

[16] Zolfaghari A, Chen T, Allen YY. Additive manufacturing of precision optics at micro and nanoscale. Int J Extreme Manuf 2019;1(1):012005.

[17] Krieger KJ, Bertollo N, Dangol M, Sheridan JT, Lowery MM, O'Cearbhaill ED. Simple and customizable method for fabrication of high-aspect ratio microneedle molds using low-cost 3D printing. Microsyst Nanoeng 2019;5(1):1–14.

[18] Lamont AC, Alsharhan AT, Sochol RD. Geometric determinants of in-situ direct laser writing. Sci Rep 2019;9(1):1–12.

[19] Zhou X, Hou Y, Lin J. A review on the processing accuracy of two-photon polymerization. AIP Adv 2015;5(3):030701.

[20] LaFratta CN, Baldacchini T. Two-photon polymerization metrology: characterization methods of mechanisms and microstructures. Micromachines 2017;8(4):101.

[21] Cardenas-Benitez B, Eschenbaum C, Mager D, Korvink JG, Madou MJ, Lemmer U, De Leon I, Martinez-Chapa SO. Pyrolysis-induced shrinking of three-dimensional structures fabricated by two-photon polymerization: experiment and theoretical model. Microsyst Nanoeng 2019;5(1):1–13.

[22] Xia C, Pan Z, Zhang S, Polden J, Wang L, Li H, Xu Y, Chen S. Model predictive control of layer width in wire arc additive manufacturing. J Manuf Process 2020;58:179–86.

[23] Wang Y, Lu J, Zhao Z, Deng W, Han J, Bai L, Yang X, Yao J. Active disturbance rejection control of layer width in wire arc additive manufacturing based on deep learning. J Manuf Process 2021;67:364–75.

[24] Yaseer A, Chen H. Machine learning based layer roughness modeling in robotic additive manufacturing. J Manuf Process 2021;70:543–52.

[25] J. Jiang C. Yu X. Xu Y. Ma J. Liu, Achieving better connections between deposited lines in additive manufacturing via machine learning, Math Biosci Eng 17 (4).

[26] Rossi A, Moretti M, Senin N. Layer inspection via digital imaging and machine learning for in-process monitoring of fused filament fabrication. J Manuf Process 2021;70:438–51.

[27] Khanzadeh M, Tian W, Yadollahi A, Doude HR, Tschopp MA, Bian L. Dual process monitoring of metal-based additive manufacturing using tensor decomposition of thermal image streams. Addit Manuf 2018;23:443–56.

[28] Seifi SH, Tian W, Doude H, Tschopp MA, Bian L. Layer-wise modeling and anomaly detection for laser-based additive manufacturing. J Manuf Sci Eng 2019;141(8):081013.

[29] Khanzadeh M, Dantin M, Tian W, Priddy MW, Doude H, Bian L. Fast prediction of thermal data stream for direct laser deposition processes using network-based tensor regression. J Manuf Sci Eng 2021:1–39.

[30] García-Moreno A-I, Alvarado-Orozco J-M, Ibarra-Medina J, Martínez-Franco E. In-process monitoring of the melt-pool motion during continuous-wave laser metal deposition. J Manuf Process 2021;65:42–50.

[31] Egan DS, Ryan CM, Parnell AC, Dowling DP. Using in-situ process monitoring data to identify defective layers in Ti-6Al-4V additively manufactured porous biomaterials. J Manuf Process 2021;64:1248–54.

[32] C. Yu J. Jiang , A perspective on using machine learning in 3D bioprinting, Int J Bioprinting 6 (1).

[33] Jiang J, Xiong Y, Zhang Z, Rosen DW. Machine learning integrated design for additive manufacturing. J Intell Manuf 2020:1–14.

[34] Q. Huang H. Nouri K. Xu Y. Chen S. Sosina T. Dasgupta , Statistical predictive modeling and compensation of geometric deviations of three-dimensional printed products, J Manuf Sci Eng 136 (6).

[35] He K, Zhang Q, Hong Y. Profile monitoring based quality control method for fused deposition modeling process. J Intell Manuf 2019;30(2):947–58.

[36] Jin Y, Qin SJ, Huang Q. Modeling inter-layer interactions for out-of-plane shape deviation reduction in additive manufacturing. IISE Trans 2020;52(7):721–31.

[37] Zhu Z, Anwer N, Huang Q, Mathieu L. Machine learning in tolerancing for additive manufacturing. CIRP Ann 2018;67(1):157–60.

[38] Ferreira RDSB, Sabbaghi A, Huang Q. Automated geometric shape deviation modeling for additive manufacturing systems via bayesian neural networks. IEEE Trans Autom Sci Eng 2019;17(2):584–98.

[39] McGregor DJ, Rylowicz S, Brenzel A, Baker D, Wood C, Pick D, Deutchman H, Shao C, Tawfick S, King WP. Analyzing part accuracy and sources of variability for additively manufactured lattice parts made on multiple printers. Addit Manuf 2021;40:101924.

[40] Jia S, Yang Y, Kelkar VA, Rajput HS, Coariti ACS, Toussaint KC, Shao C. Modeling and visualization of geometric errors for hemisphere structures produced by two-photon lithography. URL. Jan 2021. https://doi.org/10.21981/D4EK-0304. https://nanohub.org/resources/tplvaranlz.

[41] Rasmussen CE, Williams CK. Gaussian processes for machine learningVol. 1. Cambridge: MIT press; 2006.

[42] H. Zhao R. Jin S. Wu J. Shi , PDE-constrained gaussian process model on material removal rate of wire saw slicing process. J Manuf Sci Eng 133 (2).

[43] Jin R, Chang C-J, Shi J. Sequential measurement strategy for wafer geometric profile estimation. IIE Trans 2012;44(1):1–12.

[44] Plumlee M, Jin R, Roshan Joseph V, Shi J. Gaussian process modeling for engineered surfaces with applications to si wafer production. Stat 2013;2(1):159–70.

[45] Suriano S, Wang H, Shao C, Hu SJ, Sekhar P. Progressive measurement and monitoring for multi-resolution data in surface manufacturing considering spatial and cross correlations. IIE Trans 2015;47(10):1033–52.

[46] Shao C, Ren J, Wang H, Jin JJ, Hu SJ. Improving machined surface shape prediction by integrating multi-task learning with cutting force variation modeling. J Manuf Sci Eng 2017;139(1):011014.

[47] Yang Y, Shao C. Spatial interpolation for periodic surfaces in manufacturing using a Bessel additive variogram model. J Manuf Sci Eng 2018;140(6):061001.

[48] Chen H, Yang Y, Shao C. Multi-task learning for data-efficient spatiotemporal modeling of tool surface progression in ultrasonic metal welding. J Manuf Syst 2021;58:306–15.

[49] Yang Y, Dong Z, Meng Y, Shao C. Data-driven intelligent 3D surface measurement in smart manufacturing: review and outlook. Machines 2021;9(1):13.

[50] Denlinger ER, Heigel JC, Michaleris P, Palmer T. Effect of inter-layer dwell time on distortion and residual stress in additive manufacturing of titanium and nickel alloys. J Mater Process Technol 2015;215:123–31.

[51] Huang Q, Wang Y, Lyu M, Lin W. Shape deviation generator—a convolution framework for learning and predicting 3-d printing shape accuracy. IEEE Trans Autom Sci Eng 2020;17(3):1486–500.

[52] Cressie N, Wikle CK. Statistics for spatio-temporal data. John Wiley & Sons; 2015.

[53] Fletcher R. Practical methods of optimization. John Wiley & Sons; 2013.

[54] He Z, Lee Y-H, Chanda D, Wu S-T. Adaptive liquid crystal microlens array enabled by two-photon polymerization. Opt Express 2018;26(16):21184–93.

[55] Waheed S, Cabot JM, Macdonald NP, Lewis T, Guijt RM, Paull B, et al. 3D printed microfluidic devices: enablers and barriers. Lab Chip 2016;16(11):1993–2013.

[56] Ladner IS, Cullinan MA, Saha SK. Tensile properties of polymer nanowires fabricated via two-photon lithography. RSC Adv 2019;9(49):28808–13.

[57] Everitt BS, Skrondal A. The Cambridge dictionary of statistics. Cambridge University Press; 2010.

[58] Canny J. A computational approach to edge detection. IEEE Trans Pattern Anal Mach Intell 1986;6:679–98.

[59] D. Kroon , Numerical optimization of kernel based image derivatives, Short Paper University Twente.

[60] Zhang L, Wang K, Chen N. Monitoring wafers' geometric quality using an additive Gaussian process model. IIE Trans 2016;48(1):1–15.

[61] Aye S, Heyns P. An integrated Gaussian process regression for prediction of remaining useful life of slow speed bearings based on acoustic emission. Mech Syst Signal Process 2017;84:485–98.

[62] Yang Y, Shao C. Hybrid multi-task learning-based response surface modeling in manufacturing. J Manuf Syst 2021;59:607–16.

[63] Yang Y, McGregor DJ, Tawfick S, King WP, Shao C. Hierarchical data models improve the accuracy of feature level predictions for additively manufactured parts. Addit Manuf 2022;51:102621. https://doi.org/10.1016/j.addma.2022.102621.